Permeability and storativity of binary mixtures of high- and low-porosity materials

Y. Bernabé[1], U. Mok[2], B. Evans[2] and F.J. Herrmann[3]

[1]Institut de Physique du Globe, Université Louis Pasteur - CNRS, Strasbourg, France

[2]Department of Earth, Atmospheric and Planetary Sciences, Massachusetts Institute of Technology, Cambridge

[3]Department of Earth and Ocean Sciences, University of British Columbia, Vancouver, British Columbia, Canada

Abstract. As a first step towards determining the mixing laws for the transport properties of rocks, we prepared binary mixtures of high- and low-porosity materials by isostatically hot-pressing mixtures of calcite and quartz fine-grain powders. We measured the permeability and storativity of these materials using the oscillating flow technique. We systematically varied the effective pressure and the period and amplitude of the input pressure oscillation. Control measurements were performed using the steady-state flow and pulse decay techniques. They showed good agreement with the oscillating flow tests. The results reveal a high sensitivity of the hydraulic properties to the volume fraction of the high-porosity quartz-phase. Below a critical quartz content, thought to be slightly less than 20 weight-%, the quartz-aggregate inclusions were disconnected and the overall permeability was low. Above the critical quartz content (or, in other words, above the percolation threshold), the high-permeability inclusions formed a through going connected path and permeability increased sharply. We numerically simulated fluid flow through binary materials and found that permeability should approximately obey a percolation-based mixing law, consistent with the measured permeability of the calcite-quartz samples. In addition, the simulations suggested that, near the percolation threshold, oscillating flow measurements of permeability should yield decreasing values with increasing oscillation frequency. We indeed observed that changing the input frequency affected the measurements in samples above the critical quartz content but the effect was not at all that predicted by the numerical simulations.

1. Introduction

One striking characteristic of crustal rocks is their strongly heterogeneous nature at all observable scales. However, numerical modeling of geologic formations and/or processes requires rather coarse discretization. Thus arises the problem of assigning "effective" values of the rock properties to the grid-blocks, i.e., averaging out the finer scales of heterogeneity. Determining the effective physical properties of heterogeneous materials is also of great interest in mechanical engineering and applied physics (e.g., see *Hashin*'s [1983] classic review of the theory of composite materials).

Among the various physical properties of rocks, hydraulic permeability is particularly challenging. One reason is that, in nature, rock permeability ranges over more than 11 orders of magnitude [e.g., *Brace*, 1980], vastly exceeding the limits of the classic small fluctuations approach. It is also well known that permeability does not obey a simple averaging rule [e.g., *Cushman*, 1986; *Dagan*, 1986; *Durlofsky*, 1991, 1992; *Neuman*, 1994; *Renard and de Marsily*, 1997].

Here, our goal is to show that one essential ingredient to include in the mixing law for permeability is the connectivity of the high-permeability heterogeneities. However, this statement is somewhat ambiguous in the general case of a continuous distribution of permeability. Therefore, following a well-established procedure in applied physics, we started in the present paper by considering the simplest possible case, i.e., binary mixtures. Note that binary materials are interesting in their own right. They can serve as templates for bimodal geological formations such as sand-shale sequences [e.g., *Desbarats*, 1987; *Rubin*, 1995].

Clearly, the effective permeability of a binary mixture must be low (respectively, high) if the high-permeability phase forms isolated inclusions (respectively, a through going connected path). *Herrmann and Bernabé* [2004] recently proposed a model of the elastic properties of binary mixtures based on the percolation principle described above and using cluster statistics from percolation theory [*Kirkpatrick*, 1973; *Stauffer and Aharony*, 1992]. We adapted the Herrmann-Bernabé (HB) model to fluid permeability and, in an attempt to test it, fabricated synthetic rock-like materials that can be described as binary mixtures of high-

and low-permeability phases. Three varieties were prepared with different volume fractions of the two phases. We cored samples of each variety and measured their permeability and storativity using the oscillating flow method [*Kranz et al.*, 1990; *Fischer*, 1992; *Faulkner*, 1997; *Larive*, 2002] under varying effective pressure conditions and with different input periods and amplitudes.

In a seminal study, *Kamath et al.* [1992] demonstrated that time-dependent flow could be used in the laboratory to characterize the spatial variations of permeability in rock core-plugs. Indeed, an apparent decrease of permeability with increasing frequency was observed in several previous studies [*Fischer and Paterson*, 1992; *Faulkner*, 1997; *Larive*, 2002]. In principle, this should not happen in homogeneous, isotropic, pressure-insensitive materials. Hence, the binary materials mentioned above give us the opportunity to test the relation between frequency dependence and heterogeneity (for example, we speculate that frequency sensitivity should be maximum near the percolation threshold). Frequency dependence of permeability could be also used to quantify heterogeneity in the field. For example, harmonic pumping tests with variable frequency has been proposed to characterize fractured formations [*Jouanna*, 1992].

The paper is organized as follows. The materials are described in section 2 and the experimental procedures in section 3. In section 4, we report the experimental results. Section 5 is devoted to numerical modeling. The percolation-based mixing law and the frequency effect are discussed in section 6 and some conclusions are drawn in section 7. The HB model is described in the Appendix.

2. Materials

As a part of an on-going investigation of the effect of secondary phases on the mechanical properties of calcite aggregates, *Xiao and Evans* [2004] recently prepared three large blocks of porous calcite-quartz aggregates with different proportions of the two minerals (namely, 90-10, 80-20 and 70-30 weight % of calcite and quartz, respectively). Fine calcite and quartz powders (grain size < 10 μm) were mixed and subjected to a process called hot isostatic pressing (HIP) at 200 MPa pressure and 700°C in room-dry conditions. It turns out that the

quartz grains tended to form small clumps during mixing, presumably due to electrostatic forces. It is believed that clumping should not occur if the powders were saturated with a pH = 3 solution (i.e., corresponding to zero surface charge in quartz; e.g., *Revil and Glover* [1997]). But that procedure was not employed because of the high solubility of calcite in acidic solutions.

Owing to a large difference in HIP kinetics between calcite and quartz, the quartz clumps remained largely uncompacted during the HIP stage while the surrounding calcite matrix tightly densified. Thus, the final materials consisted of high-porosity inclusions embedded in a low-porosity matrix, as confirmed by examining polished sections of the hot-pressed materials under the scanning electron microscope (SEM) in back-scattered electron mode. Figure 1 shows SEM micrographs of the 90-10 and 70-30 materials. In both cases, the quartz inclusions consist of sharply angular, 6-12 μm large grains and relatively large (3-6 μm), inter-granular pores. On the other hand, the calcite matrix shows a typical grain-growth microstructure (i.e., enlarged 10-50 μm grains and sub-micron pores located at the three-grain edges), consistent with the observations of *Bernabé et al.* [1982] on pure hot-pressed calcite.

We cored several samples from the three blocks mentioned above and precisely ground them to a cylindrical shape. For reasons that will be made clear latter, two sample sizes were used. The S-samples (i.e., 90-10S, 80-20S, 70-30S1 and 70-30S2) had a length of 19.8-20.1 mm and a diameter of 10.0 mm, whereas the L-samples (i.e., 90-10L, 80-20L and 70-30L) were 38.0-38.2 mm in length and 19.0 mm in diameter. We measured the connected porosity ϕ_c of each sample using Archimedes method (see Table 1).

3. Experimental Procedures

After jacketing of the sample between two axially bored end-pieces, the sample assembly was inserted in the pressure vessel, connected to the upstream and downstream vents and hydrostatically loaded. For the S-samples, we increased the confining pressure P_c by steps starting at 30 MPa while keeping pore pressure P_p constant at 20 MPa (the loading sequence used for each sample can be seen in Figure 2; no measurements were made during unloading). At each pressure step, we performed a series of oscillating flow tests. We varied the period T

of the input pressure oscillation between 10 and 480 s and the input amplitude A_U between 0.1 and 1.0 MPa. We also ran a number of control tests using the steady-state flow and pressure pulse methods.

We discovered that the downstream reservoir storage was too large compared to that of the S-samples to allow precise determination of storativity [*Bernabé et al.*, 2004]. Unfortunately, our set-up was such that it was essentially impossible to decrease the size of the downstream reservoir. We tried instead to use larger samples (i.e., the L-samples) for which storativity was measurable. Since investigating the pressure sensitivity of calcite-quartz aggregates was not our main goal we did not vary the pressure conditions for the L-samples (P_c = 50 MPa and P_p = 20 MPa). This simplified procedure gave us more time to explore a greater frequency range than with the S-samples.

Since the oscillating flow method has been presented in details in previous studies [e.g., *Kranz et al.*, 1990; *Fischer*, 1992; *Faulkner*, 1997; *Larive*, 2002], we will only give a brief description here. An oscillation of the upstream pressure (amplitude A_U and period T) is generated using a computer-controlled pump and the resulting pressure oscillation in the downstream reservoir is recorded. The early-time transient is discarded and Fourier analysis is applied to the late-time downstream signal. A very sharp peak is obtained at the same frequency as the input (i.e., upstream) oscillation. After all frequencies except the peak frequency are filtered out, the downstream oscillation is found attenuated and phase-shifted with respect to the input signal. We denote $A = A_D/A_U<1$ the downstream to upstream amplitude ratio and $\varphi = \varphi_D-\varphi_U>0$ the phase-shift (the subscripts D and U refer to the downstream and upstream oscillations, respectively). In the case of a homogeneous material, the flow configuration is effectively one-dimensional. The late-time solution of the one-dimensional, Fourier-transformed, flow equation with the appropriate boundary conditions (see section 5.2) is [*Kranz et al.*, 1990; *Fischer*, 1992]:

$$Ae^{-i\varphi} = \left[\frac{1+i}{\sqrt{\alpha}}\sinh\left((1+i)\sqrt{\frac{\alpha}{\beta}}\right) + \cosh\left((1+i)\sqrt{\frac{\alpha}{\beta}}\right)\right]^{-1} \qquad (1).$$

The dimensionless parameters α and β in equation (1) are defined by:

$$\alpha = \frac{SL\beta}{\gamma_D}, \qquad \beta = \frac{STk}{\eta L \gamma_D} \tag{2},$$

where S is the sample cross-section area, L the sample length, β the sample storativity, γ_D the downstream reservoir storage, k the sample permeability and η the fluid viscosity. Note that *Fischer* [1992] used different dimensionless parameters, $\alpha = \gamma_D/SL\beta$ and $\beta = L(\eta\beta/Tk)^{1/2}$, which allow rewriting equation (1) in a slightly nicer form. The use of β is disadvantageous however, because β depends on both storativity and permeability. Therefore, α and β cannot be interpreted as independent material properties.

Equation (1) is highly non-linear and must be solved numerically for α and β, usually using some kind of optimization method. Once α and β are determined, k and β can be calculated using equations (2). Here, we applied a method developed by *Bernabé et al.* [2004] that allows estimating the uncertainty on k and β assuming the experimental uncertainty on A and α.

4. Results

4.1. Effective pressure dependence

The values of k measured for the S-samples are shown in Figure 2 as functions of effective pressure $P_{eff} = P_c - P_p$. Notice that ensemble-averaged values were plotted in Figure 2 (the measurements were repeated 3 to 6 times) and that the vertical bars indicate plus or minus two standard deviations. The first observation is that k increased significantly with quartz content (see also Table 1). A second observation is the moderate pressure sensitivity of permeability. Interestingly, the pressure sensitivity of k increases with quartz content, implying that the pores are more deformable within the quartz inclusions than inside the calcite matrix. This is consistent with the pore microstructure observed in Figure 1. The pores in the quartz inclusions tend to be more elongated than those in the calcite matrix.

4.2. Frequency dependence

First of all, we emphasize that neither permeability nor storativity can really be frequency dependent in the range of frequencies used here (inertial effects arise at much higher

frequencies, on the order of tens of kHz; e.g., *Johnson et al.* [1987]). However it is entirely possible that, in the heterogeneous, moderately pressure-sensitive materials considered here, changing the input period affects the quantities measured in an oscillating flow test, i.e., the amplitude ratio A and phase-shift φ. Since the standard interpretation method does not include any correction for this kind of effect, an apparent dependence of k and φ on frequency may then be observed. Thus, this section is devoted to describing the effect of frequency on "apparent" k and φ. Note that the term "apparent" will be omitted but always implied hereafter.

In order to examine the effect of frequency, we plotted k and φ measured on the L-samples (i.e., the simple optimization solutions of equation (1) indicated by gray dots in Figure 3) as functions of T. Furthermore, we estimated the k and φ uncertainties [*Bernabé et al.*, 2004] assuming an uncertainty on A of 0.001 and a time resolution $\delta t = 0.2$ s, leading to a phase shift uncertainty equal to $2\pi\delta t/T$. The results of this uncertainty analysis are shown in Figure 3 where the error bars represent the entire range of possible k and φ values and the open diamonds indicate the geometric averages (note that, except for the longest periods, they nearly coincide with the optimization solutions). We see that the uncertainty on k and φ strongly increases for T lower than 30 s. This is consistent with the observed increasing variability of the S-sample measurements (indicated by stars in Figure 3) at decreasing T and the fact that we experienced serious difficulties to control the upstream pump at very small periods and generate an accurate sinusoidal signal. The relative uncertainty was much larger on φ than on k, a common observation in oscillating flow studies [e.g., *Takahashi*, 2003] and a consequence of an overly large downstream reservoir [*Bernabé et al.*, 2004]. Moreover, we performed very long flow tests on the L-samples, allowing us to run the Fourier analysis in moving time-windows. We thus checked that, except for the longest periods, early-time transients had enough time to die out and did not influence the measured values of A and φ. However, in long-period measurements, the early-time transients most likely led to systematic overestimations of A and/or underestimations of φ. We tried to take this into account and applied a range of reasonable corrections to the A and φ values, resulting in a significant

increase of the estimated k and ϕ uncertainties and the discrepancy between corrected and uncorrected values (compare the open diamonds and gray dots in Figure 3 for $T > 300$ s).

Figure 3 displays a rather complex and, as will be discussed later, unexpected frequency dependence of both k and ϕ. Within the estimated uncertainty, the 90-10L sample did not display any significant effect of frequency on permeability and storativity, but the 80-20L and 70-30L samples behaved quite differently. In both samples, k and ϕ decreased with increasing period, eventually reached a minimum and increased again. These variations were more pronounced for 70-30L than 80-20L. We verified that the S-samples exhibited the same behavior as described above. A direct comparison was possible for the measurements performed at $P_{\text{eff}} = 30$ MPa. In the other cases, we had to remove the effect of pressure. The entire set of pressure-corrected data-points is plotted in Figure 3, showing that the frequency effects reported above were consistently observed in all samples and under all pressure conditions. Finally, as expected in heterogeneous materials, different samples of the same material variety turned out to have slightly different permeabilities. The fact that the permeability of the L-samples was systematically higher than that of the S-samples is puzzling. But, in view of the small number of samples considered here, this may merely have been a coincidence.

5. Numerical simulations

The flow equation in a heterogeneous, porous medium is:

$$\frac{\partial}{\partial x}\left(\frac{k}{\phi}\frac{\partial P_{\text{p}}}{\partial x}\right)+\frac{\partial}{\partial y}\left(\frac{k}{\phi}\frac{\partial P_{\text{p}}}{\partial y}\right)+\frac{\partial}{\partial z}\left(\frac{k}{\phi}\frac{\partial P_{\text{p}}}{\partial z}\right)=\phi\frac{\partial P_{\text{p}}}{\partial t} \qquad (3),$$

where P_{p}, k and ϕ are functions of the space coordinates x, y and z. In a binary material, k and ϕ can only take two possible values (denoted k_1, k_2, and ϕ_1, ϕ_2, respectively). Omitting the early-time transient in an oscillating flow test, we can rewrite equation (3) in the Fourier domain as:

$$\frac{\partial}{\partial x}\left(\frac{k}{\phi}\frac{\partial P}{\partial x}\right)+\frac{\partial}{\partial y}\left(\frac{k}{\phi}\frac{\partial P}{\partial y}\right)+\frac{\partial}{\partial z}\left(\frac{k}{\phi}\frac{\partial P}{\partial z}\right)=i\omega\phi P \qquad (4),$$

where $\omega = 2\pi/T$ is the angular frequency and P is a complex scalar function giving the amplitude and phase of the late-time pressure oscillations at any point in the sample. The upstream, downstream and lateral boundary conditions are respectively written:

$$P_{x=L} = A_{\mathrm{U}} \tag{5},$$

$$i\omega\beta_{\mathrm{D}} P_{x=0} = \iint_S \frac{k_{x=0}}{\mu} \left(\frac{\partial P}{\partial x}\right)_{x=0} dS \tag{6},$$

and

$$\frac{\partial P}{\partial y} = \frac{\partial P}{\partial z} = 0 \qquad \text{(along the sides)} \tag{7}.$$

Equation (5) defines the input pressure oscillation, equation (6) expresses the fluid volume balance in the downstream reservoir, and equation (7) states that the sample is enclosed in an impermeable jacket. We rewrite equations (4-7) in dimensionless form:

$$\frac{\partial}{\partial x}\left(\frac{\partial P}{\partial x}\right) + \frac{\partial}{\partial y}\left(\frac{\partial P}{\partial y}\right) + \frac{\partial}{\partial z}\left(\frac{\partial P}{\partial z}\right) = 2i\omega P \tag{8},$$

$$P_{x=L} = 1 \tag{9},$$

and

$$2iP_{x=0} = \iint_S \lambda^2 \left(\frac{\partial P}{\partial x}\right)_{x=0} dS \tag{10},$$

where x, y and z now denote normalized space coordinates (i.e., divided by L), S represents the normalized cross-section area, $\lambda^2 = L^2/S$ is a measure of the sample aspect ratio, and equation (7) remains unchanged.

The system above can be solved numerically as follows. 1) We consider a (two- or three-dimensional) rectangular grid and randomly distribute phase 1 and phase 2 over the (square or cubic) grid-blocks according to the probabilities p_1 and $p_2 = 1 - p_1$ (i.e., the volume fractions of phase 1 and phase 2, respectively). 2) Equations (8) and (10) are discretized using a standard centered finite-difference scheme (including standard implementation of the upstream and lateral boundary conditions). We obtain a system of linear equations, whose unknowns are

the (complex) values of P at the center of each grid-block. 3) We invert the (complex) matrix of this system using Cholesky decomposition or the conjugate gradient method depending on the size of the matrix (i.e., the number of grid-blocks). An example of a two-dimensional realization corresponding to $p_1 = 0.35$ (with $\sigma_1<\sigma_2$ and $\sigma_1<\sigma_b$) is shown in Figure 4 as well as the resulting amplitude and phase fields (i.e., absolute value and argument of P). We observed that, for p_1 near 1 or 0, the contour lines in the amplitude and phase fields were regularly distributed, nearly straight, vertical lines. But, as illustrated in Figure 4, the amplitude and phase fields became irregular and intricate for p_2 near the percolation threshold of the high-permeability phase. In order to interpret the results of these simulations in terms of effective κ and ϕ (i.e., effective, dimensionless permeability and storativity), we recorded $P = Ae^{-i\theta}$ on the downstream face and tried to solve equation (1) as was done for the physical oscillating flow measurements. This turned out to be a difficult and time-consuming exercise (because of the existence of relative minima, the initial parameters of the optimization algorithm had to be adjusted for each individual cases). As a consequence, we had to limit the number of realizations to about 10 for each p_1 considered. To remedy this deficiency, we also performed steady-state simulations. In this case, the ϕ-term disappears and equation (8) only depends on the permeability ratio, $k_1/k_2 = \sigma_1/\sigma_2$. Note that the finite-difference version of equation (8) is equivalent to the Kirchoff equations in a square (or cubic) network where the conductance between two connected nodes (i.e., the centers of two touching grid-blocks) is given by the harmonic average of κ in the corresponding grid-blocks. This analogy allowed us to utilize previously implemented network simulation programs. We could thus consider two-dimensional square and three-dimensional cubic lattices, significantly increase the size of the networks up to 50x50x50 and the number of realizations to 500, and explore a larger range of permeability ratio (i.e., σ_1/σ_2 from 10^{-1} to 10^{-6}).

5.1. Effective Permeability

The results of two-dimensional oscillating flow simulations with $\sigma_1 = 0.001$, $\sigma_2 = 1.$, $\sigma_l = 0.01$ and $\sigma_2 = 0.1$ are displayed in Figure 5. The dots represent the ensemble geometric average of κ (Figure 5a) and the arithmetic average of ϕ (Figure 5b). The fluctuations of κ and ϕ are indicated by the vertical line segments (i.e., they connect the minimum and

maximum of the set of values corresponding to each volume fraction p_2). We can see that the fluctuations are small for p_2 close to 0 or 1, and become large near the percolation threshold of the high-permeability phase (i.e., 0.59 in two dimensional square grids). We see in Figure 5a that, for p_2 up to about 0.55, the effective κ (i.e., dimensionless permeability) closely follows the two-dimensional, lower Hashin-Shtrikman (HS) bound [*Hashin and Shtrikman*, 1962] and then increases sharply to finally join the upper HS bound for p_2 approaching 1. This behavior is in excellent agreement with the HB model with the exponent equal to 0.5 (see the Appendix).

The steady-state, two- and three-dimensional flow simulations fully concurred with Figure 5a. This is illustrated in Figure 6 showing the steady-state results for 10x10x10 and 50x50x50 networks and for $\kappa_1/\kappa_2 = 10^{-4}$, superposed on the three-dimensional HS bounds and the HB model (with an exponent of 0.9). We can see that the fluctuations of κ decrease with increasing network size and become very small in 50x50x50 networks (except near the percolation threshold). However, we point out that the conjugate gradient method used with the large networks did not always converge. Some of the realizations were therefore rejected, thus introducing an unknown bias in the statistics of κ. The number of rejected realizations was very small for p_2 near 0 or 1 and for κ_1/κ_2 near unity, but reached 20 % near the percolation threshold for $\kappa_1/\kappa_2 = 10^{-6}$. In addition, we examined the distribution of κ as a function of p_2. For p_2 near zero or one, κ displayed approximately Gaussian distributions. In small networks, for p_2 near the percolation threshold, we observed bimodal distributions, reflecting the fact that, in individual realizations, κ was predominantly dependent on the connectivity of the high-κ phase. In large networks, the bimodal character disappeared, although the distributions of κ were still not Gaussian. We obtained similar results for permeability ratios as low as 10^{-6}.

5.2. Effective Storativity

Storativity can be expressed as follows [*Brace et al.*, 1968; *Zimmerman*, 1991]:

$$\sigma = C_B + \phi_c C_F \approx (1 + \phi_c) C_G \qquad (11),$$

where C_B is the drained bulk compressibility of the material, C_F the fluid compressibility and C_G the compressibility of the mineral grains forming the material. The third term on the right-hand side is very small compared to the other ones and can be neglected. The second term is proportional to porosity and therefore obeys a linear mixing law. The first term accounts for the change in pore volume dV_p accompanying a change in pore pressure dP_p. We can write $dV_p = dV_p^{(1)}+dV_p^{(2)}$, where the superscripts refer to the phases. This leads to $C_B dP_{eff} = p_1 C_B^{(1)} dP_{eff}^{(1)}+p_2 C_B^{(2)} dP_{eff}^{(2)}$, where dP_{eff}, $dP_{eff}^{(1)}$ and $dP_{eff}^{(2)}$ denote the average changes in effective stress induced by dP_p in the binary mixture and in both phases, respectively. In the description reported at the beginning of section 5, the hydraulic equations are not supplemented by mechanics equations expressing the stress changes in the solid portion of the material. This is equivalent to implicitly assume that $dP_{eff} = dP_{eff}^{(1)} = dP_{eff}^{(2)} = -dP_p$, which may not always be adequate in real situations (e.g., see consolidation theory [*Domenico and Schwartz*, 1990]). This leads to an additive mixing rule for C_B. Hence, in the numerical simulations, α must satisfy $\alpha = p_1\alpha_1+p_2\alpha_2$ (or $\alpha = p_1\alpha_1+p_2\alpha_2$). However Figure 5b shows significant downward deviations for p_2 near the percolation threshold. We verified that this discrepancy substantially decreased when we increased α_1 and α_2 while keeping α_1/α_2, β_1 and β_2 constant, which, from equation (2), is equivalent to increasing the period T. Hence, the numeric simulations produced a frequency effect, although a quite different one to that shown in Figure 3. In the numerical simulations, α tends to decrease with decreasing T.

5.3. Frequency Dependence

Decreasing T in oscillating flow measurements on a single sample can be simulated by considering a single realization and calculating A and α for decreasing values of α_1 and α_2 while keeping α_1/α_2, β_1 and β_2 constant. Unfortunately, interpreting A and α in terms of β and α was so much time-consuming, that we were unable to examine a sufficiently large number of realizations to obtain statistically meaningful results. However a number of qualitative observations were made. In general, we found that both β and α decreased with decreasing T. This effect was stronger near the percolation threshold than for p_2 close to 1 or 0. But very large fluctuations occurred from one realization to another (especially near the percolation threshold). We even noted cases where β and α slightly increased with decreasing T. We

suspect that the magnitude of the frequency effect diminishes as T is increased and eventually vanishes below some critical frequency, which we were unfortunately unable to identify. We considered two kinds of mixture, those in which ϕ and k were directly related (i.e., $\phi_1 < \phi_2$ implies $k_1 < k_2$), and those with an inverse k-ϕ relation (i.e., $\phi_1 < \phi_2$ implies $k_1 > k_2$). We found that the frequency dependence was significant only in mixtures with a direct k-ϕ relation, which suggests that ϕ and k tend to play opposite roles.

In order to assess the validity of these results, we tested the accuracy of the finite difference scheme by running purely homogeneous cases and comparing their results to equation (1). Even in grids as small as 44x22, the results agreed with equation (1) within less than 1% for ω/ϕ down to 0.02 (the discrepancy grew to 5% for ω/ϕ = 0.01). All the simulations mentioned above were performed with a minimum ω/ϕ at least 10 times greater than that last value.

6. Discussion

6.1. Mixing laws

According to the considerations above, we assume an approximately linear mixing law for ϕ and a percolation-based model for k (see the Appendix). Note that the same kind of percolation-based model could be used for $1/C_B$, but the percolation threshold is not the same as before (i.e., the binary mixture is incompressible if the incompressible, low-permeability phase is connected). Using such a model for $1/C_B$ is not justified here since all the samples are far above the percolation threshold for incompressibility.

First of all, we must check whether or not our experimental results are consistent with these two mixing laws. We simplified this task by using "characteristic" values of ϕ_c, ϕ and k (see Table 1). For ϕ_c, we only had the previously mentioned bench-top measurements, while, for ϕ and k, we selected measurements performed at P_{eff} = 30 MPa and in an intermediate range of T (namely, the entire range for 90-10, 20 to 80 s for 80-20 and 10 to 60 s for 70-30). We thus estimated not only average values of k and ϕ, but also the corresponding two standard deviation ranges. We then proceeded in three steps: 1) we guessed the values of the porosity of the pure phases, $\phi_c^{(calcite)}$ and $\phi_c^{(quartz)}$. Examination of micrographs such as those shown in

Figure 1 helped us select a porosity ratio, $\phi_c^{(calcite)}/\phi_c^{(quartz)}$ of about 0.2 and a value of $\phi_c^{(calcite)}$ agreeing with previously published results on hot-pressed calcite [*Bernabé et al.*, 1982; *Zhang et al.*, 1994]. These values allowed us to estimate plausible volume fractions $p^{(calcite)}$ and $p^{(quartz)}$ in all samples (see Figure 7a). 2) We plotted the measured values of ϕ as a function of $p^{(quartz)}$ and verified that the data-points approximately followed a linear mixing law (see Figure 7b). This line defined $\phi^{(calcite)}$ and $\phi^{(quartz)}$. We indeed found reasonable values, which confirmed that the quartz-phase was significantly more deformable than the calcite-phase. 3) We finally plotted the measured values of k as a function of $p^{(quartz)}$ and compared them to the HB model with a value for $k^{(calcite)}$ constrained by $\phi_c^{(calcite)}$ and the results of *Zhang et al.* [1994], and with $k^{(quartz)}$ determined by trials and errors (see Figure 7c). Note that, for the HB model, we used a percolation threshold of 0.20, consistent with continuous percolation [e.g., *Kirkpatrick*, 1973], and an exponent of 0.7 slightly smaller than that of the three-dimensional simulations.

Although we can see that the experimental results are consistent with the percolation-based HB model, we realize that they do not, by themselves, prove its validity. Indeed, data for only three values of $p^{(quartz)}$ are available, while much more would be needed (especially near the percolation threshold) in order to draw definitive conclusions. To our knowledge, there are no other laboratory measurements of the fluid permeability of binary mixtures reported in the literature. However, fluid permeability is, in many ways, analogous to electrical conductivity. *Landauer* [1952] analyzed previously published data on the electrical conductivity of binary alloys. In Figure 8, we compare laboratory measurements of the electrical conductivity of Bi-Bi_2 Pb, Bi-Sn and Mg_2 Pb-Pb alloys [*Landauer*, 1952, and references therein] to the HB model. We can see that these data also give good support to the HB model. The other alloys investigated by *Landauer* [1952] were examined too. We do not show the corresponding results here because their conductivity contrasts were very small, but we can state that they did agree well with the HB model. Of course, other models (e.g., self-consistent, *Landauer* [1952], or Keller's reciprocity theorem, *del Rio et al.* [1998]) can also produce an acceptable fit with these experimental data. But we argue that only a percolation-based model can match the S-shaped mixing lines, which characterize the binary alloys data as well as the flow simulations presented in section 5.1. It is interesting to note that the model

proposed by *del Rio et al.* [1998] is based on the assumption that the mixing law is symmetric with respect to an exchange of the phases. Such a symmetry assumption is incompatible with a percolation-based model since the connectivity of the high-conductivity phase is important whereas that of the low-conductivity phase is irrelevant.

How can we generalize the percolation-based mixing law described in the Appendix, to heterogeneous media with continuous distributions of permeability? We cannot answer this question at present. However, we anticipate that the method known as critical path analysis [e.g., *Ambegaokar et al.*, 1971; *Pollak*, 1972; *Friedman and Seaton*, 1998; *Hunt*, 2001] and the concept of critical permeability (i.e., the maximum permeability k_c, for which a through going path with $k > k_c$ exists) will probably be central to the solution of this problem.

Another feature of the percolation-based HB model is the existence of a power-law singularity at the percolation threshold (approached from above). The presence of a singularity could be important in certain applications (e.g., a singularity in the elastic properties acts as a reflector for seismic waves [*Herrmann and Bernabé*, 2004]). Two questions thus arise: 1) do the experimental and numerical data prove or disprove the existence of such a singularity? 2) If the singularity exists, what is the value of its exponent b? Concerning the first question, we can state that even the experimental data of *Landauer* [1952] are too scarce to draw definitive conclusions, but that, at first sight, the numerical results of Figure 6b suggest a smooth mixing law for permeability. Nevertheless, Figure 6b is not, in our opinion, incompatible with a singularity for two reasons. a) The singularity is not necessarily located exactly on the lower HS bound as assumed in the HB model (see the Appendix). Indeed, it is well known that the accuracy of the HS bounds diminishes when the inclusion density increases. b) The fluctuations are quite large near the percolation threshold (and may, in fact, be even larger since a number of realizations were rejected as explained in section 5.1).

Despite the fact that we cannot reach a definite conclusion regarding the existence of a singularity, we can nevertheless observe that the HB model adequately fits the experimental and numerical data. We therefore need to consider the second question, i.e., estimate the exponent b. For the two- and three-dimensional simulations (Figures 5a and 6b), a good fit

was obtained with $b = 0.5$ and 0.9, respectively. The HB model with $b = 0.7$ matched very well our experimental data (Figure 7c) whereas a smaller value, $b = 0.5$, appeared to be needed for the electrical conductivity data (Figure 8). These values are significantly larger than the values originally proposed in the HB model (i.e., 0.14 and 0.41 in two and three dimensions, respectively). Indeed, the HB model assumes that every high-permeability inclusion attached to the infinite, percolation cluster does contribute equally to the effective permeability (see the Appendix). The volume fraction of high-permeability material used in the higher HS bound is thus given by the strength of the infinite percolation cluster (proportional to $(p - p_c)^b$ with $b = 0.14$ or 0.41, in two or three dimensions, respectively [e.g., *Stauffer and Aharony*, 1992]). *Kirkpatrick* [1973] reported very large conductivity exponents, namely, 1.3 and 1.6 in two and three dimensions, respectively, based on earlier studies where mixtures of a conducting phase and a perfect insulator were considered. In a conductor-insulator mixture, it is clear that the dead-end branches attached to the infinite percolation cluster do not carry any current. Hence, only the backbone of the infinite percolation cluster should be counted, thus yielding an exponent of 1.6 or 1.7 in two or three dimensions, respectively [e.g., *Isichenko*, 1992]. However we argue that, if the low-conductivity phase is not a perfect insulator, then the dead-end branches of the percolation cluster must carry some current and cannot be totally discounted. Thus, it is reasonable to conclude that b should lie between the extreme values mentioned above (i.e., 0.41 and 1.7 in three dimensions) as we indeed found in the various cases examined. It would be very interesting to find out if b approaches the conductor-insulator values mentioned above when the conductivity contrast grows to infinity. Answering this question is a very difficult task, out of the scope of the present paper.

One final remark on this topic must be made. According to percolation theory, the power law behavior only holds in the close vicinity of the percolation threshold (approached from above). The exponent b defines the order of the singularity and may not characterize the behavior far from the percolation threshold. Here however, we were unable to establish the existence of a singularity and the exponent b was adjusted to maximize the fit of the HB model with the experimental or numerical data for all volume fractions. Therefore, our

estimated values of b do not characterize the singularity itself (if it exists) but the entire mixing law. This remark is important in any situation where the sharpness of the singularity is a relevant parameter (e.g., seismic reflector [*Herrmann and Bernabé*, 2004]). The singularity is sharp for $b < 1$ and the sharpness increases with decreasing b. The point we are trying to make here is that a sharp singularity may still exist even if the globally defined exponent b is large.

6.2. Frequency dependence

The numerical results of section 5 suggest that an apparent increase of permeability and storativity with decreasing frequency should be observed in heterogeneous materials. Instead we observed a relatively well resolved decrease of k and α with decreasing frequency, followed by a more uncertainty increase. We do not know how to explain this discrepancy at the present time. We did find, however, that, in agreement with the numerical simulations, the frequency effect was significant near the percolation threshold (i.e., in 80-20 and 70-30 materials) and vanished away from it (i.e., in 90-10). It is possible that the downstream reservoir storage in our apparatus is too large to allow accurate measurement of storativity (indeed, we obtained unphysical, negative values of α in the 80-20S, 70-30S1 and 70-30S2 samples). But this is not a sufficient explanation for permeability varied by 25 % in the 80-20L sample and by 18 % in 70-30L, significantly more than the expected uncertainty on k.

This kind of frequency effect is poorly documented in the literature. *Fischer and Paterson* [1992] reported a permeability decrease in Solnhofen limestone of nearly one order of magnitude when T was lowered from 8000 to 200 s but offered no explanation for the phenomenon. They also observed that the permeability variations increased when the amplitude of the input oscillation was raised. *Faulkner* [1997] further verified that the frequency effect was present only when the amplitude of the input oscillation was not negligible with respect to the mean effective pressure, which suggests that the phenomenon is linked to the pressure sensitivity of the rocks investigated (in this case equation (3) becomes non-linear). Here, we did not notice any effect of the input amplitude and the materials displayed only moderate effective pressure sensitivity. However, effective pressure sensitivity may have played a role in our experiments. In other studies the frequency

dependence of permeability was inexistent or much weaker and only occurring for very small input periods [e.g., *Larive*, 2002].

7. Conclusion

Our main goal was to determine the effective permeability and storativity of binary mixtures with variable volume fractions of the high- and low-permeability phases. Based on a combination of experimental and numerical results, we propose that permeability should approximately obey the percolation-based, HB mixing law described in details in the Appendix. Below the percolation threshold (i.e., when the high-permeability phase is disconnected) the effective permeability is given by the lower Hashin-Shtrikman bound. Above the percolation threshold, we apply the upper HS bound to a portion of the high-permeability phase belonging to the infinite cluster and the residual mixed material.

In the numerical simulations, storativity was treated as an additive property like porosity and therefore followed a linear mixing law. In the moderately pressure-sensitive materials used here, a linear mixing law was also approximately verified, but this conclusion should not be generalized to strongly pressure-sensitive materials such as fractured rocks.

Finally, the numerical simulations revealed that, in the most heterogeneous materials (i.e., near the percolation threshold), the measured values of permeability and storativity should decrease with increasing input frequency. This effect has indeed been observed in previous oscillating flow studies. However, the fact that the frequency effect was enhanced by raising the amplitude of the input oscillation, suggests that pressure-sensitivity might have played a more important role than heterogeneity. Here, we observed a rather unexpected behaviour, namely, a decrease of permeability and storativity with decreasing frequency followed by a poorly resolved increase. We cannot offer an explanation for this surprising behaviour at present. We did however notice that the frequency dependence was negligible in the 90-10 material, i.e., the farthest away from the percolation threshold.

Acknowledgements: X. Xiao provided the SEM micrographs and A. Maineult helped run the large simulations. This work was partially funded by the US Department of Energy under grant DE-FG02-97ER14760.

Appendix

The HB model [*Herrmann and Bernabé*, 2004] can be adapted to the hydraulic flow case as follows: let us consider an infinitely large body of a binary mixture of a low-permeability (LP) and a high-permeability (HP) phase. We denote p and q =1–p the volume fractions of HP and LP, respectively. For p = 0, the body exclusively consists of the LP phase. With increasing p, HP inclusions are progressively formed until only the HP phase remains for p = 1. At a critical volume fraction p_c (i.e., the percolation threshold) an infinite, connected HP cluster is formed. However, for $p \geq p_c$, not all HP inclusions belong to the infinite cluster. Isolated HP inclusions can still be found, embedded in the remaining LP material and forming with it a mixture (M). Percolation theory predicts that, in the vicinity of the percolation threshold, the volume fraction p^* of HP material that belongs to the infinite cluster is zero for $p < p_c$ and has a power law dependence on $(p - p_c)$ for $p \geq p_c$ [*Stauffer and Aharony*, 1992]. For convenience, we assume that this power law extends all the way to p = 1. Hence, for $p \geq p_c$, p^* is given by:

$$p^* = p\left(\frac{p - p_c}{1 - p_c}\right)^b \qquad \text{(A1)},$$

where the exponent b is a positive, real number, which depends on spatial dimensionality, but not on the interconnection topology of the inclusions. Site percolation theory predicts b = 0.14 and 0.41 in two- and three-dimensional discrete lattices, respectively [*Stauffer and Aharony*, 1992]. Below p_c, the volume fraction of the mixed material M is given by $q^* = (1 - p^*)$. For modelling M, we need the volume fractions of its LP and HP parts, $q_M = (1 - p)/\{(1 - p) + (p - p^*)\}$ and $p_M = (1 - q_M)$, respectively. We obtain:

$$p_M = 1 - \frac{q}{1 - p\left(\frac{p - p_c}{1 - p_c}\right)^b} \qquad \text{(A2)}.$$

We assume that the binary mixture is statistically isotropic. We argue that the permeability (or the electrical conductivity) of a statistically isotropic material consisting of isolated inclusions randomly distributed inside a continuous (connected) matrix can be accurately estimated using the HS bounds [*Hashin and Shtrikman*, 1962]. The upper HS bound must be used when the HP phase forms the connected matrix while the lower one applies otherwise. Accordingly, below p_c, k is given by the lower HS bound:

$$k = k_{LP} + \frac{p}{\frac{1}{k_{HP} - k_{LP}} + \frac{q}{3k_{LP}}} \qquad \text{(A3)}.$$

Above p_c we must switch to the higher HS bound:

$$k = k_{HP} + \frac{q^*}{\frac{1}{k_M - k_{HP}} + \frac{p^*}{3k_{HP}}} \qquad \text{(A4)},$$

where k_M is the permeability of the mixed material M. Since the HP inclusions in M are isolated, k_M is calculated using the lower HS bound:

$$k_M = k_{LP} + \frac{p_M}{\frac{1}{k_{HP} - k_{LP}} + \frac{q_M}{3k_{LP}}} \qquad \text{(A5)}.$$

Note that equations (A3) to (A5) are valid in three dimensions. In two-dimensional cases, we must simply change the value of the constant from 3 to 2.

Finally, if it were demonstrated that only part of the infinite cluster controlled the value of the effective permeability (see discussion in section 6.1), the HB model could still be applied provided that the appropriate value of the exponent b was used.

References

Ambegaokar, V.N., B.I. Halperin, and J.S. Langer, Hopping conductivity in disordered systems, *Phys. Rev. B*, *4*, 2612-2620, 1971.

Bernabé, Y., W.F. Brace, and B. Evans, Permeability, porosity and pore geometry of hot-pressed calcite, *Mech. Mat.*, *1*, 173-183, 1982.

Bernabé, Y., U. Mok, and B. Evans, A note on the oscillating flow method for measuring rock permeability, submitted to *Int. J. Rock Mech. Min. Sci. & Geomech. Abstr.*, 2004.

Brace, W.F., Permeability of crystalline and argillaceous rocks, *Int. J. Rock Mech. Min. Sci. Geomech. Abstr.*, *17*, 241-251, 1980.

Brace, W.F., J.B. Walsh, and W.T. Frangos, Permeability of granite under high pressure, *J. Geophys. Res.*, *73*, 2225-2236, 1968.

Cushman, J.H., On measurement, scale and scaling, *Water Resour. Res.*, *22*, 129-134, 1986.

Dagan, G., Statistical theory of groundwater flow and transport: pore to laboratory, laboratory to formation, and formation to regional scale, *Water Resour. Res.*, *22*, 120S-134S, 1986.

Del Rio, J.A., R.W. Zimmerman, and R.A. Dawe, Formula for the conductivity of a two-component material based on the reciprocity theorem, *Solid State Comm.*, *4*, 183-186, 1998.

Desbarats, A.J., Numerical estimation of effective permeability in sand-shale formations, *Water Resour. Res.*, *23*, 273-286, 1987.

Domenico, P.A., and F.W. Schwartz, *Physical and Chemical Hydrogeology*, John Wiley & Sons, New York, pp.824, 1990.

Durlofsky, L.J., Numerical calculation of equivalent grid block permeability tensors for heterogeneous porous media, *Water Resour. Res.*, *27*, 699-708, 1991.

Durlofsky, L.J., Representation of grid block permeability in coarse scale models of randomly heterogeneous porous media, *Water Resour. Res.*, *28*, 1791-1800, 1992.

Faulkner, D.R., *The Role of Clay-bearing Fault Gouges in Controlling Fluid Pressures in Fault Zones: Implications for Fault Mechanics*, Ph.D. Thesis, University of Manchester, U.K., pp. 279, 1997.

Fischer, G.J., The determination of permeability and storage capacity: pore pressure oscillation method, in *Fault Mechanics and Transport Properties of Rocks*, edited by B. Evans and T.-f. Wong, pp. 187-211, Academic Press, New York, 1992.

Fischer, G.J., and M.S. Paterson, Measurements of permeability and storage capacity in rocks during deformation at high temperature and pressure, in *Fault Mechanics and Transport*

Properties of Rocks, edited by B. Evans and T.-f. Wong, 213-252, Academic Press, New York, 1992.

Friedman, S.P., and N.A. Seaton, Critical path analysis of the relationship between permeability and electrical conductivity of three-dimensional pore networks, *Water Resour. Res.*, *34*, 1703-1710, 1998.

Hashin, Z., Analysis of composite materials - a survey, *ASME J. Appl. Mech.*, *50*, 481-505, 1983.

Hashin, Z., and S. Shtrikman, A variational approach to the theory of the effective magnetic permeability of multiphase materials, *J. Appl. Phys.*, *33*, 3125-3131, 1962.

Herrmann, F.J., and Y. Bernabé, Seismic singularities at upper mantle phase transitions: a site percolation model, submitted to *Geophys. J. Int.*, 2004.

Hunt, A.G., Applications of percolation theory to porous media with distributed local conductances, *Adv. Water Resour.*, *24*, 279-307, 2001.

Isichenko, M.B., Percolation, statistical topography, and transport in random media, *Rev. Mod. Phys.*, *64*, 961-1043, 1992.

Johnson, D.L., J. Koplik, and R. Dashen, Theory of dynamic permeability and tortuosity in fluid-saturated porous media, *J. Fluid Mech.*, *176*, 379-402, 1987.

Jouanna, P., Access to stochastic fractured media characteristics by harmonic hydraulic pumping, *Int. J. Rock Mech. Min. Sci. & Geomech. Abstr.*, *29*, 83-87, 1992.

Kamath,J., R.E., Boyer, and F.N. Nakagawa, Characterization of core-scale heterogeneities using laboratory transients, *SPE Formation Evaluation*, *7*, 219-227, 1992.

Kirkpatrick, S., Percolation and conduction, *Rev. Mod. Phys.*, *45*, 574-588, 1973.

Kranz, R.L., J.S. Saltzman, and J.D. Blacic, Hydraulic diffusivity measurements on laboratory samples using an oscillating pore pressure method, *Int. J. Rock Mech. Min. Sci. & Geomech. Abstr.*, *27*, 345-352, 1990.

Landauer, R., The electrical resistance of binary metallic mixtures, *J. Appl. Phys.*, *23*, 779-784, 1952.

Larive, E., *Etude expérimentale des roches à très faible perméabilité par la mise en œuvre d'un perméamètre de précision* (in French), Ph.D. Thesis, Université de Montpellier II, France, pp. 183, 2002.

Pollak, M.A., Percolation treatment of dc hopping conduction, *J. Non-Cryst. Solids*, *11*, 1-24, 1972.

Renard, P., and G. de Marsily, Calculating equivalent permeability: a review, *Adv. Water Resour.*, *20*, 253-278, 1997.

Rubin, Y., Flow and transport in bimodal heterogeneous formations, *Water Resour. Res.*, *31*, 2461-2468, 1995.

Stauffer, D., and A. Aharony, *Introduction to Percolation Theory* (2nd. ed.), Taylor and Francis, Washington DC, pp.180, 1992.

Takahashi, M., Permeability change during experimental fault smearing, *J. Geophys. Res.*, *108*, 2235, doi:10.1029/2002JB001984, 2003.

Xiao, X., and B. Evans, Shear enhanced compaction during nonlinear viscous creep of porous calcite-quartz aggregates, in press in *Earth Planet. Sci. Lett.*, 2004.

Zimmerman, R.W., *Compressibility of Sandstones*, Elsevier, New York, pp.173, 1991.

Zhang, S., M.S. Paterson, and S.F. Cox, Porosity and permeability evolution during hot isostatic pressing of calcite aggregates, *J. Geophys. Res.*, *99*, 15741-15760, 1994.

Table 1: Measured (bold-faced) or inferred (italic) values of the properties (namely, volume fraction of the calcite-phase, connected porosity, storativity and permeability) of the various samples and pure phases. The numbers in parentheses represent two standard deviations.

sample	$p^{(calcite)}$	ϕ_c	β (10^{-11} Pa^{-1})	k (10^{-18} m^2)
90-10S	*0.97*	**0.037**	**1.5 (1.7)**	**0.9 (0.2)**
90-10L	*0.93*	**0.043**	**3.1 (0.6)**	**1.3 (0.2)**
80-20S	*0.73*	**0.070**		**9.3 (0.4)**
80-20L	*0.74*	**0.068**	**4.3 (1.0)**	**10.4 (0.2)**
70-30S1	*0.64*	**0.082**		**24.0 (0.2)**
70-30S2	*0.58*	**0.091**		**31.3 (1.7)**
70-30L	*0.64*	**0.083**	**6.6 (1.4)**	**32.0 (1.9)**
Calcite	1.	*0.033*	*2.3*	*1.*
Quartz	0.	*0.17*	*16.*	*200.*

Captions

Figure 1: SEM micrographs of polished sections of the binary materials, a) 90-10, and b) 70-30. Calcite grains appear in a light shade of gray, whereas the quartz grains are dark gray and the pores black. A 100 μm scale bar is indicated at the bottom of each micrograph.

Figure 2: Permeability of the samples 90-10S, 80-20S, 70-30S1 and 70-30S2 as a function of effective pressure (solid diamonds, arithmetic mean of the oscillating flow measurements; open circles, pulse transients; open squares, steady-state flow). The variability bars represent plus or minus two standard deviations.

Figure 3: Permeability and storativity of the S- and L-samples as a function of the input period. The gray dots (respectively, open diamonds) indicate the values obtained for the L-samples without any correction (respectively, corrected for the transient signal). The errors bars represent the total estimated uncertainty on the corrected values. The stars indicate the S-samples values after correction of the pressure effect (see text for more details).

Figure 4: An example of two-dimensional oscillating flow simulation: a) the spatial distribution of the phases (white, low-α/low-β phase with volume fraction 0.35; black, high-α/high-β phase). b) The amplitude ratio field (white indicates the maximum values and black the minimum). c) The phase-shift field (same gray code as above).

Figure 5: Results of the two-dimensional oscillating flow simulations (only the case with $\alpha_1 = 0.001$, $\alpha_2 = 1.$, $\beta_1 = 0.01$ and $\beta_2 = 0.1$ is shown here): a) Effective α (i.e., permeability) as a function of p_2. We also plotted the HS bounds (gray curves) and the HB model (black line) with the exponent $b = 0.5$ and $p_2 = 0.59$ for the percolation threshold. b) Effective β (i.e., storativity) as a function of p_2. The linear mixing curve is shown for comparison. The variability bars indicate two standard deviations.

Figure 6: Results of the three-dimensional steady-state flow simulations (only the case with $\alpha_1 = 1$ and $\alpha_2 = 10000$ is shown here) for two network size: a) 10x10x10, and b) 50x50x50. We also plotted the HS bounds (gray curves) and the HB model (black line) with the exponent $b = 0.9$ and $p_2 = 0.31$ for the percolation threshold. The variability bars indicate two standard deviations.

Figure 7: Summary of the experimental results reported in section 4. a) Connected porosity: the values for the calcite- and quartz-phase as well as the volume fractions were guessed from prior knowledge on hot-pressed calcite [*Bernabé et al.*, 1982; *Zhang et al.*, 1994] and the linearity of the mixing curve for porosity (black straight line). b) Storativity: we applied the previously determined volume fractions and estimated the storativity of the pure phases from the linearity of the mixing curve (black straight line). c) Permeability: the values for the pure phases were guessed, in part based on prior knowledge on hot-pressed calcite, and in part so that the corresponding HB mixing curve (black line) with the exponent $b = 0.7$ and a percolation threshold of 0.2 would fit the experimental data. The HS bounds (gray lines) are also plotted for comparison.

Figure 8: Electrical conductivity of binary alloys [*Landauer*, 1952]. In each case, we also plotted the HS bounds (gray curves) and the HB model (black lines) with the exponent $b = 0.5$ and $p_2 = 0.2$ for the percolation threshold.

a)

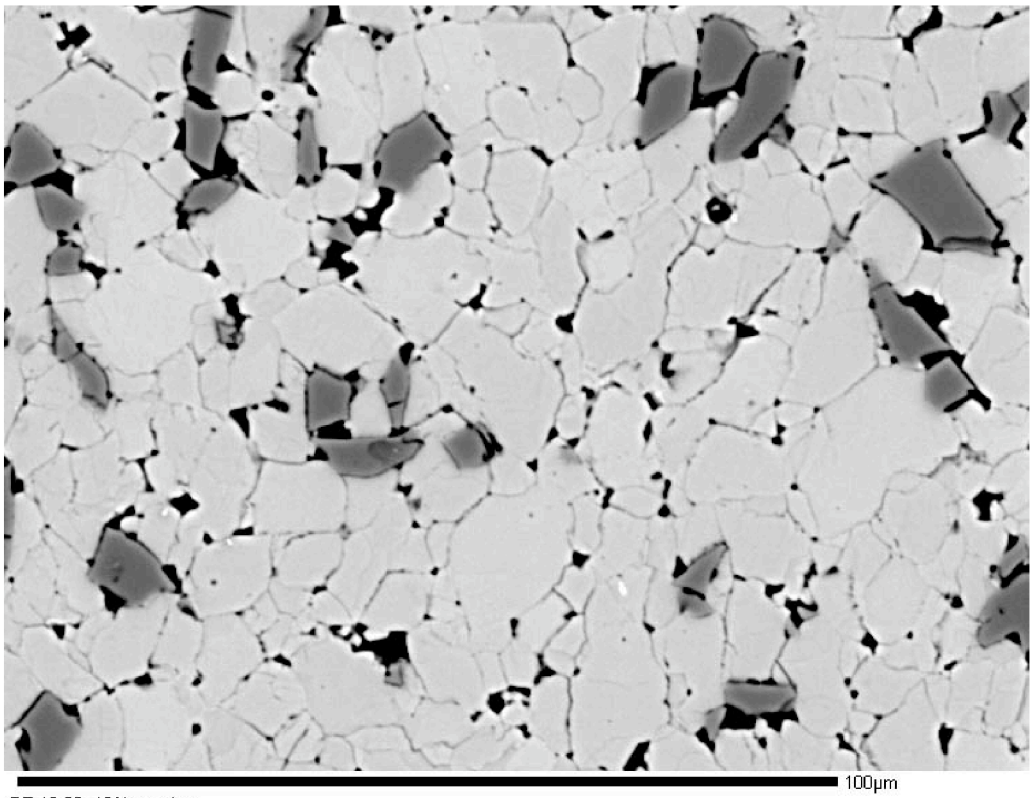

b)

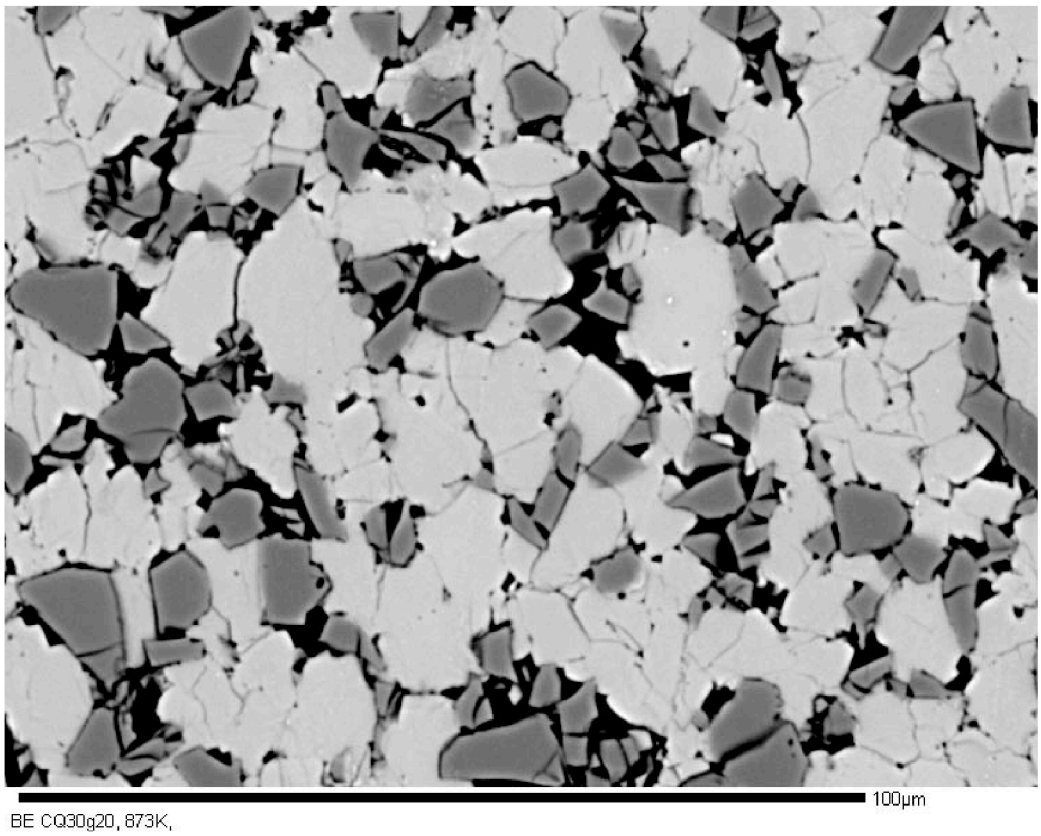

Figure 1

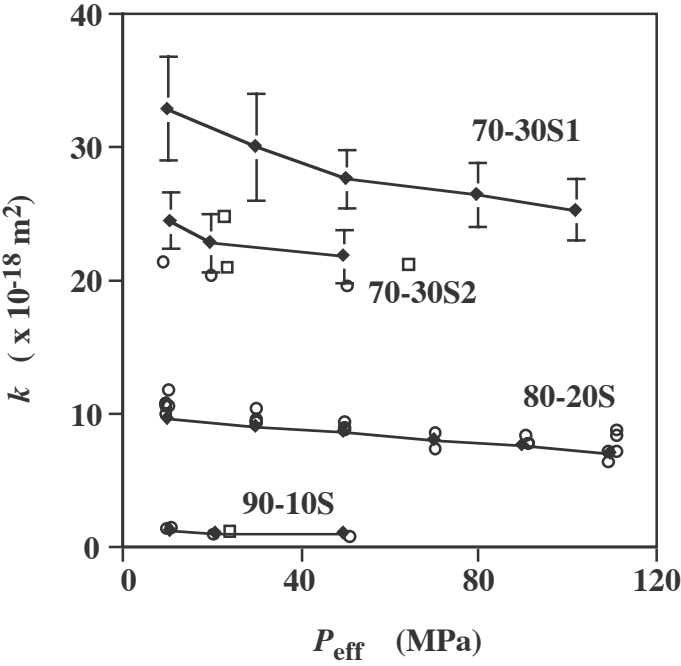
40
30
20
10
0
0
40
80
120
k (x 10-18 m2)
Peff (MPa)
70-30S1
70-30S2
80-20S
90-10S

Figure 2

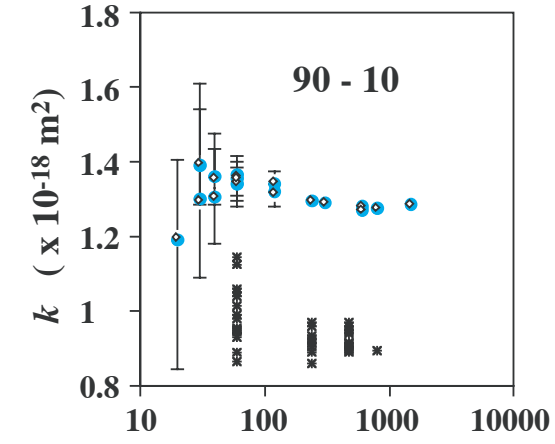

a)

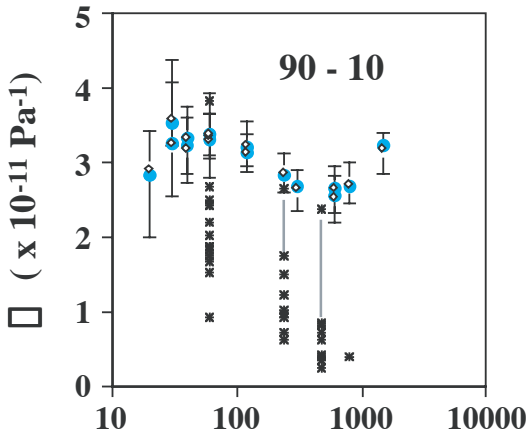

b)

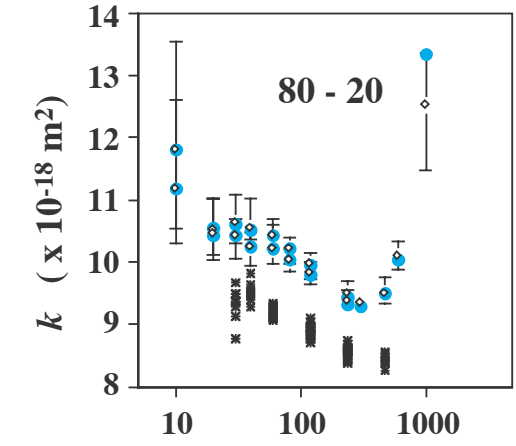

c)

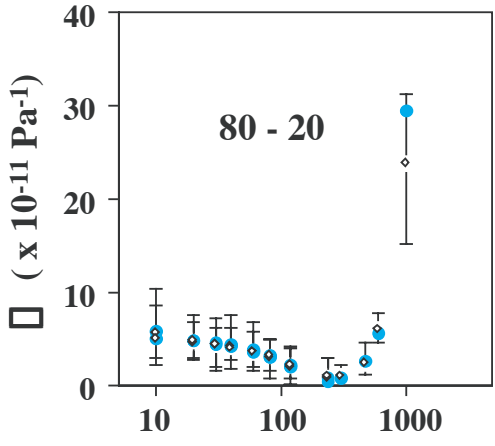

d)

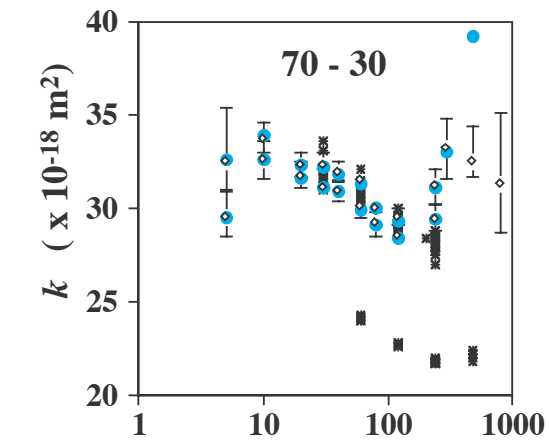

e)

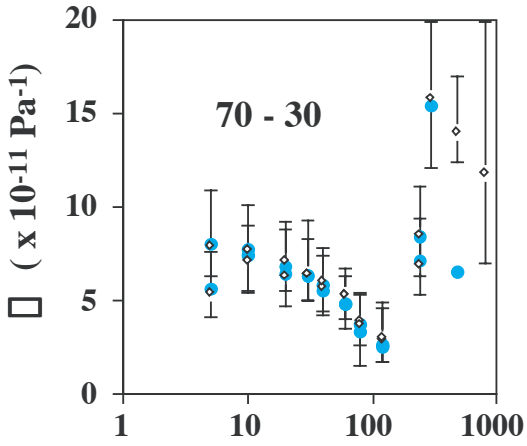

f)

Figure 3

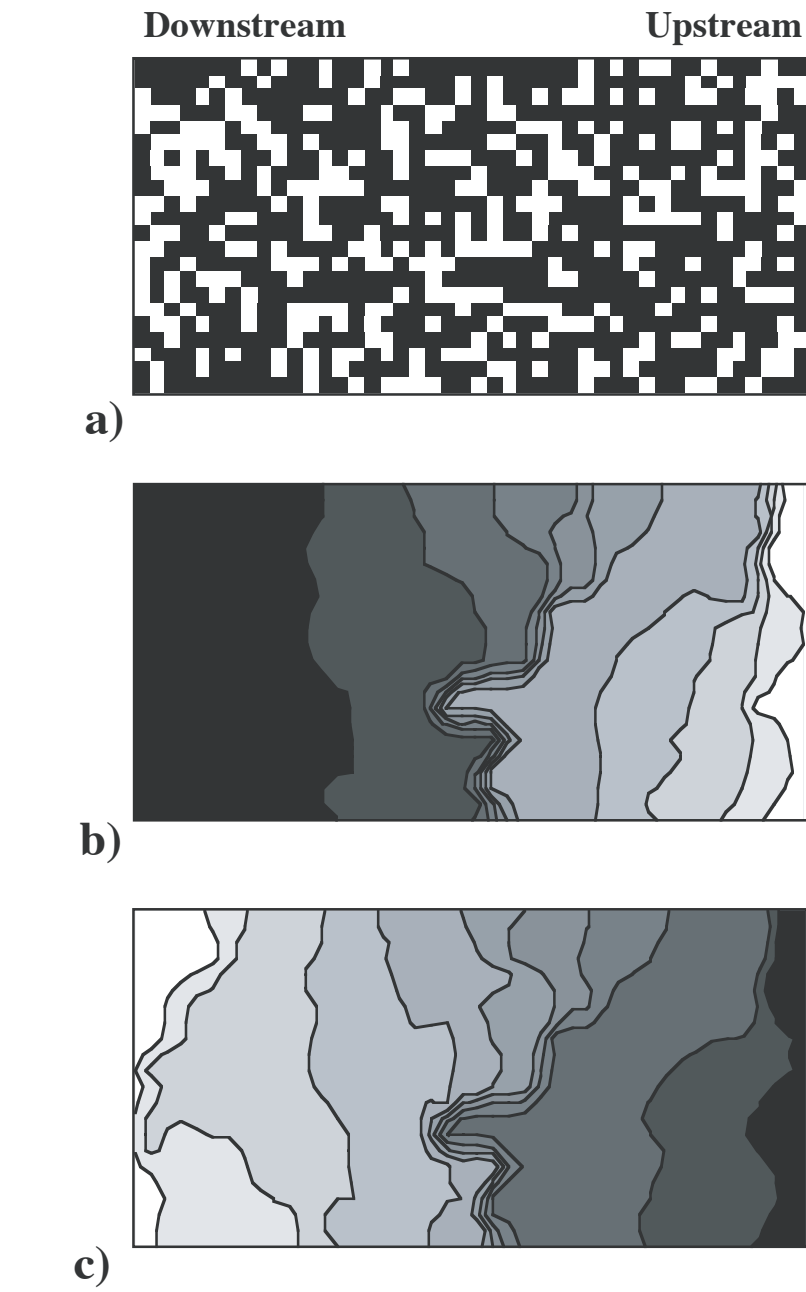

Figure 4

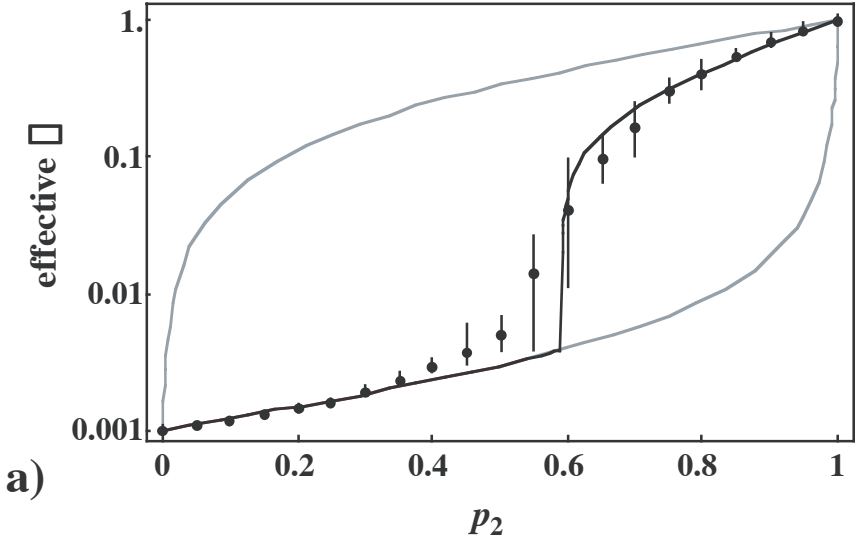
1.
0.1
0.01
0.001
effective
0
0.2
0.4
0.6
0.8
1
p_2

a)

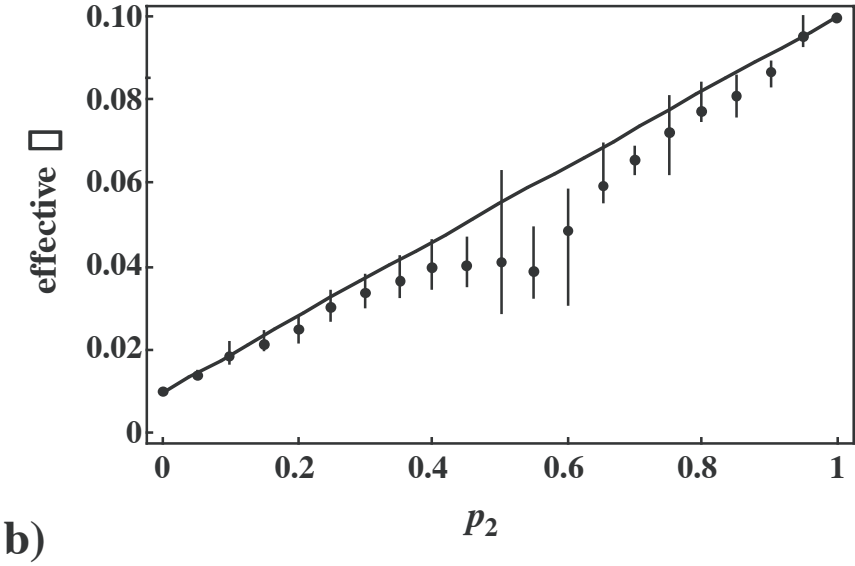
0.10
0.08
0.06
0.04
0.02
0
effective
0
0.2
0.4
0.6
0.8
1
p_2

b)

Figure 5

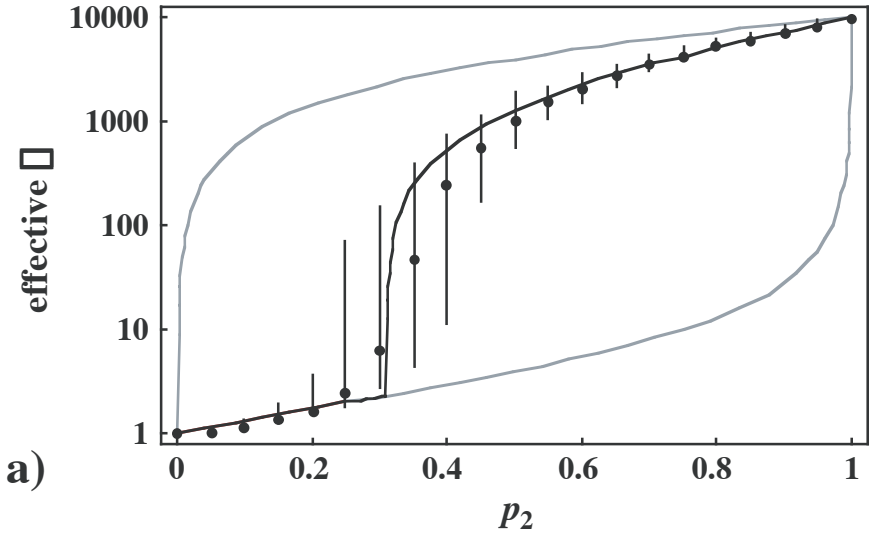
10000
1000
100
10
1
effective
0
0.2
0.4
0.6
0.8
1
p_2
a)

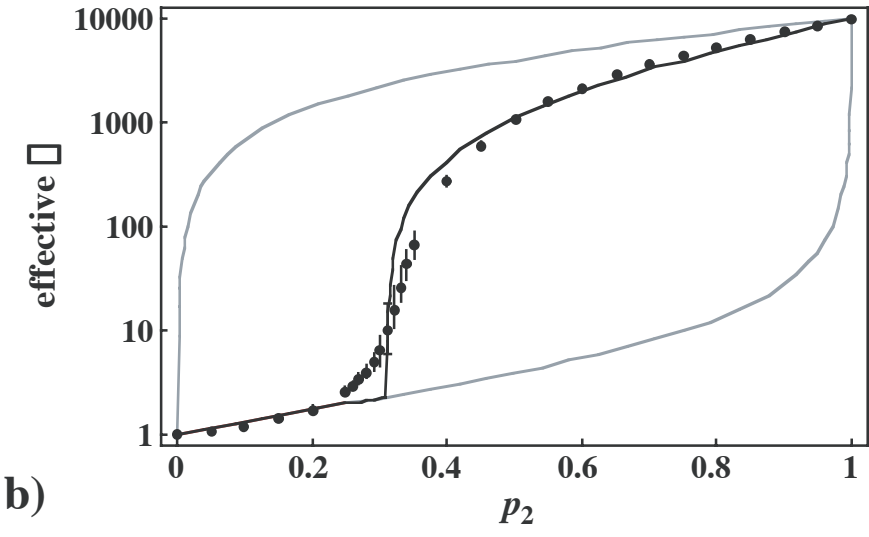
10000
1000
100
10
1
effective
0
0.2
0.4
0.6
0.8
1
p_2
b)

Figure 6

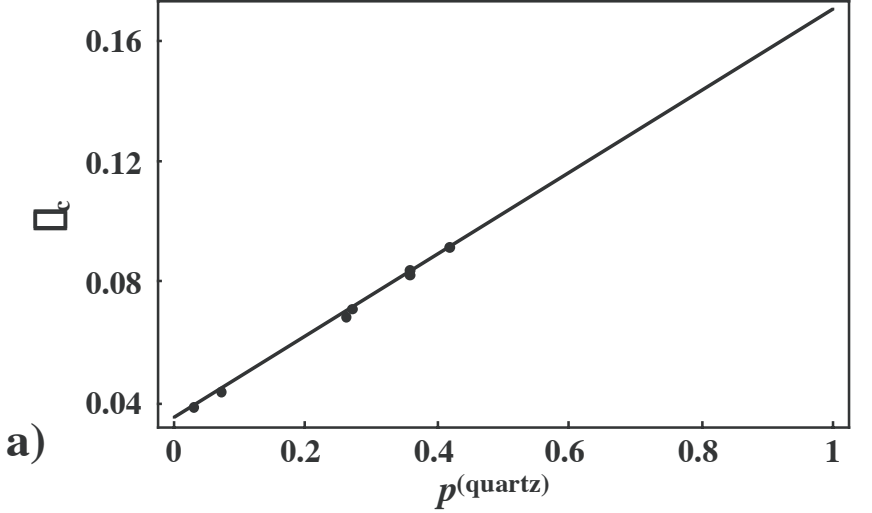
0.16
0.12
0.08
0.04
□t
a)
0
0.2
0.4
0.6
0.8
1
p(quartz)

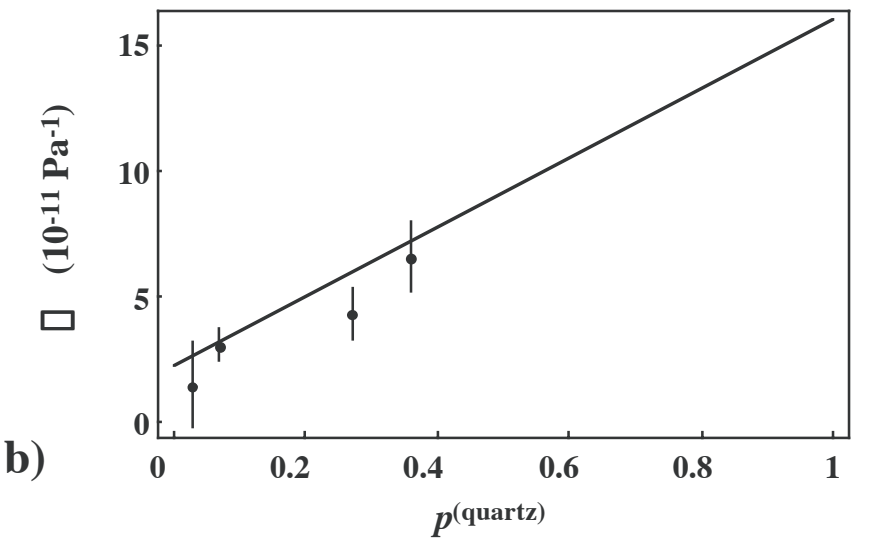
15
10
5
0
□ (10-11 Pa-1)
b)
0
0.2
0.4
0.6
0.8
1
p(quartz)

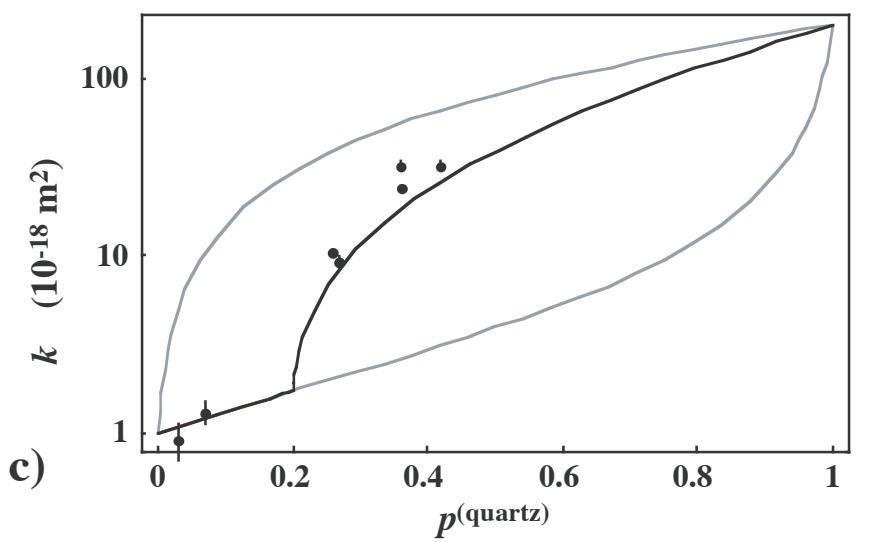
100
10
1
k (10-18 m2)
c)
0
0.2
0.4
0.6
0.8
1
p(quartz)

Figure 7

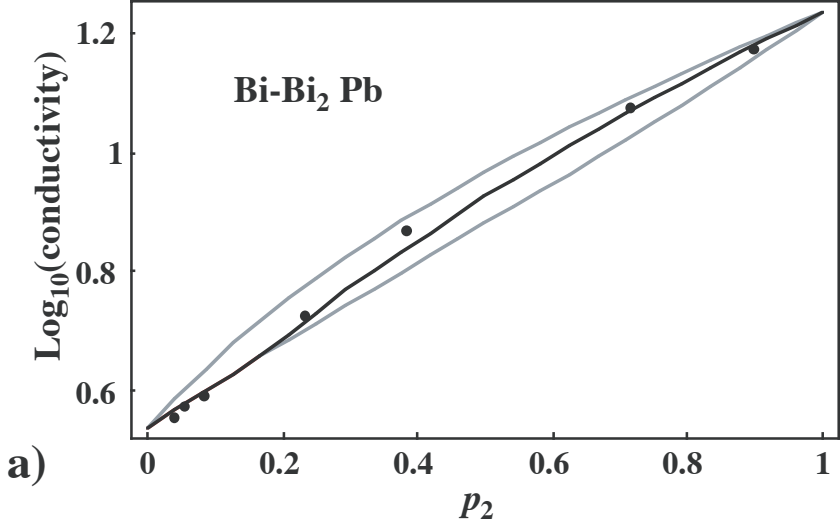

a)

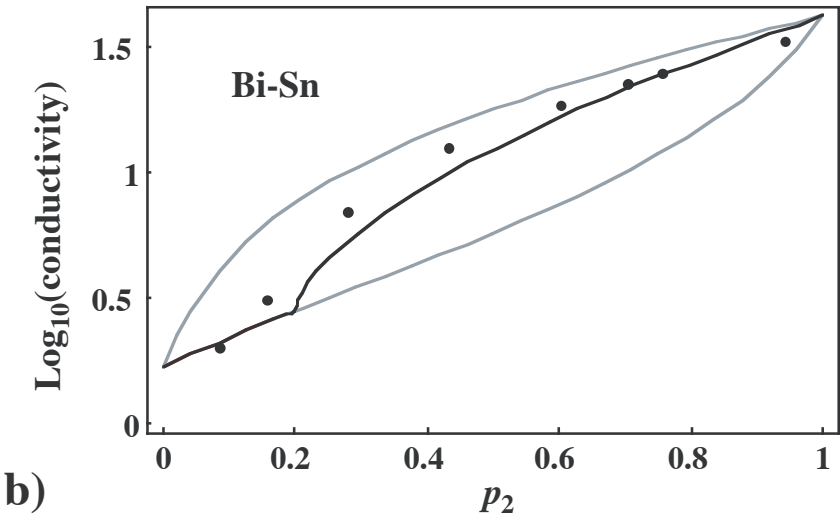

b)

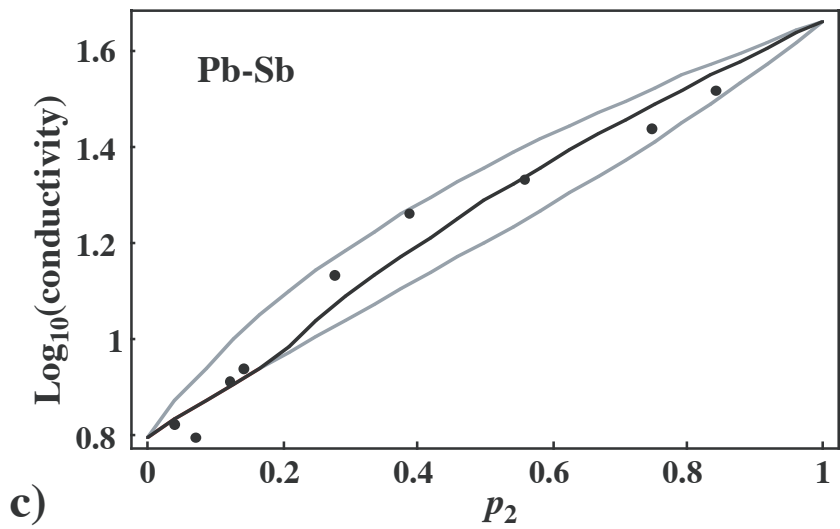

c)

Figure 8